



## Research Article

# Speed Sensorless Control Based on Initial Rotor Position Detection for EESM

Feng Cai,<sup>1</sup> Ke Li ,<sup>2</sup> and Xiaodong Sun <sup>1</sup>

<sup>1</sup>Automotive Engineering Research Institute, Jiangsu University, Zhenjiang 212013, China

<sup>2</sup>School of Electrical and Information Engineering, Jiangsu University, Zhenjiang 212013, China

Correspondence should be addressed to Ke Li; [like@ujs.edu.cn](mailto:like@ujs.edu.cn) and Xiaodong Sun; [xdsun@ujs.edu.cn](mailto:xdsun@ujs.edu.cn)

Received 16 November 2021; Accepted 23 December 2021; Published 12 January 2022

Academic Editor: Omar Naifar

Copyright © 2022 Feng Cai et al. This is an open access article distributed under the Creative Commons Attribution License, which permits unrestricted use, distribution, and reproduction in any medium, provided the original work is properly cited.

Electrically excited synchronous motor (EESM) is widely used in many large equipment drives because of its strong overload capacity, high efficiency, and adjustable power factor. The research and development of a high-performance EESM control system can realize the high combination of energy-saving speed regulation and green environmental protection and has a high social effect and economic value. In this paper, the signal injection method is used to obtain the initial rotor position information of EESM. Sliding Fourier transform is used to improve the initial position angle detection method based on the rotor signal injection method, and the improved method is compared with the traditional voltage integration method. Rotor high-frequency signal injection method was used to detect the rotor position information of the motor during operation, and the influence of the damping winding on the rotor signal injection method was analyzed. On the premise that the damping winding had no influence on the method, a method of obtaining the rotor position information of EESM without a speed sensor was designed. Finally, the speed sensorless regulation system using the initial rotor position detection method is simulated, which verifies the accuracy of the proposed speed sensorless control scheme.

## 1. Introduction

*1.1. Motivation.* With the acceleration of industrialization, high-power electric drive system plays an increasingly important role in production. In the early stage of the motor industry, DC electric drive system has the advantages of a wide speed range, good dynamic and static performance, high efficiency, simple structure, and so on, widely used in various high-performance speed control occasions. However, AC drive systems (such as asynchronous motor drive system and synchronous motor drive system) cannot be widely used because of their complicated mathematical model and difficult control. Compared with DC motor, AC motor structure is relatively simple and low cost; operation and maintenance are relatively easy and have the advantages of the strong and durable; and synchronous motor also has the advantage of power factor that can be adjusted, so they are widely used in the early period, and most of them have poor speed control ability [1–3]. With the development of

modern power electronic technology, as well as the constant maturity of ac speed regulation theory, AC drive system has become the mainstream of the entire electric drive system, widely used in various applications, especially in the field of high-power drive has played an increasingly important role [4–8].

As a multivariable, nonlinear and strongly coupled controlled object, the electromagnetic torque of an electrically excited synchronous motor (EESM) is not only related to the amplitude of the stator flux, but also to the angle between them. In order to obtain the ideal dynamic performance, it is necessary to control the flux linkage amplitude and phase at the same time. By controlling the size and direction of these space vectors, the electromagnetic torque of AC motor can be dynamically controlled in real time.

The vector control system began in the middle of the twentieth century. The vector control theory is mainly based on the control principle of induction motor field orientation

published by F. Brazchke and other scholars of Siemens in Germany, and the coordinate transformation control of induction motor stator voltage was applied by Custman and Clarke in the United States established by the patent [4, 13, 14]. The magnetic-field-oriented vector control system has decoupled the excitation component and the torque component to obtain the working characteristics such as the DC motor and has a good dynamic and static control effect. However, the direct axis reluctance and quadrature axis reluctance caused by the salient pole rotor are different, which makes the vector generated by the flux linkage different in space and time. Therefore, for the field-oriented vector control system, the real control is impossible to be completely decoupled. In practice, the accurate observation of directional flux and the variation of motor parameters will affect the performance of the magnetic field directional vector control system. These problems are the shortcomings of the magnetic field directional vector control system and need to be further studied. In the mid-1980s, the direct torque control theory was proposed by Professor M. Depenbrock of Ruhr University in Germany and Japanese scholar I. Takahashi. DTC is a new high-performance speed control theory for AC motors, which is fundamentally different from magnetic field directional control theory. DTC directly controls the stator flux and torque of a motor in the stator coordinate system [15–17]. The realization of DTC refers first to establish an off-line optimal switching table, then according to the torque and hysteresis controller designed to select the appropriate voltage space vector from the optimal switching table, and then through the inverter to output the required voltage acting on the motor stator winding.

*1.2. Related Research.* The rotor position of the motor plays an important role in the start and operation of the motor, among which the detection of the initial position angle and the rotor position of the motor operation will affect the performance of the motor speed regulation system [18–21]. The detection methods of the initial position angle of EESM can be divided into two categories: (1) the first type is to determine the initial position angle of the motor by calculating the flux angle by integrating the stator voltage. This method is based on the mathematical model of the motor, so it is suitable for most AC motors including EESM. However, in position detection, if the running time is too long under static conditions, the stator voltage numerical integration deviation will result in inaccurate measurement results [22–24]. (2) The second method uses the asymmetry of the motor to estimate the position of the corresponding induction by the signal injection method. Compared with the first method, the second method can run at rest and very low speed. This method can only be used to meet the rotor asymmetry of a specific AC motor, EESM, to meet the characteristics of rotor asymmetry, so this method can be used [25–27]. The rotor side of EESM is excited by the excitation circuit, so the signal injection method used in EESM can be divided into rotor signal injection method and stator signal injection method. In the stator signal injection

method, foreign scholars also inject low-frequency signal into the stator winding of EESM to obtain the rotor initial position, stator low frequency signal injection method can be applied to medium voltage synchronous motor.

EESM speed control system mostly adopts double closed-loop control, in which the inner ring is the current ring and the outer ring is the speed ring. The current loop needs to accurately sample the current signal for feedback to form the current closed-loop control, while the speed loop needs to accurately obtain the speed signal for feedback to form the speed closed-loop control. Among them, the speed acquisition method is mainly based on sensors, including rotary transformer, incremental encoder, and so on. In the occasion of higher requirements for speed and rotor position, there are absolute encoders, mixed absolute encoders, and so on. In the use of such devices, the following problems will be encountered in the process of installation and operation: (1) the cost of hardware increases, and the price of encoder increases with the increase of detection accuracy and environmental severity; (2) the work of the encoder will be damaged due to the influence of external environment, increasing the maintenance cost; and (3) the installation accuracy of the encoder will also affect the accuracy of detection. Due to the limitation of the above problems, more and more scholars at home and abroad are devoted to the research of speed sensorless control [28–31].

According to the author's research, the method of obtaining the rotor position of the motor is mainly based on the fundamental model of the motor. The fundamental model-based methods usually extract rotor positions from motor flux or back electromotive force (EMF). This kind of method has the advantages of simplicity and straightforwardness. In this category, there are various approaches to obtaining rotor position information. In [32], the rotor position and speed are both estimated by a sliding mode observer (SMO). In [33], the sliding-mode coefficients are tuned by an adaptive algorithm online. The position estimation error caused by voltage source inverter (VSI) nonlinearity can thus be reduced. In [34], a full-order SMO is designed to obtain the extended EMF (EEMF). Compared to the EMF, the EEMF can be detected even at extremely low speeds. The sensorless scheme based on EEMF can reverse motor speed without any position sensor. In addition to the SMO, the other observers such as Luenberger observer (LO) [35], extended Kalman filter (EKF) [36–38], and model reference adaptive system (MRAS) [39] are also employed for position estimation. In [39], a speed observer that combines artificial intelligence and MRAS is proposed, which is associated with the control scheme as sensorless algorithms for rotor speed and flux estimation under low-speed regions for induction motors.

*1.3. Contributions.* The main contributions of this paper are that the signal injection method is used to obtain the initial rotor position information of EESM, and the sliding Fourier transform is used to improve the initial position angle detection method. At the same time, the improved method is compared with the traditional voltage integration method.

On the other hand, the rotor high-frequency signal injection method was used to detect the rotor position information of the motor during operation, and the influence of the damping winding on the rotor signal injection method was analyzed. On the premise that the damping winding had no influence on the method, a method of obtaining the rotor position information of EESM without a speed sensor was designed.

**1.4. Paper Organization.** The paper is organized as follows. First, the mathematical model of EESM is described in Section 2. Section 3 describes the principle of speed sensorless control based on initial rotor position detection for EESM. The simulation results are presented in Section 4. Finally, the conclusion is given in Section 5.

## 2. Mathematical Model of EESM

In the control system of electrically excited synchronous motor, the coordinate transformation is needed to realize decoupling and calculation of motor mathematical model. Commonly used coordinate systems are ABC synchronous motor natural coordinate system, the two-phase static  $\alpha$ - $\beta$  coordinate system, the two-phase rotating  $d$ - $q$  coordinate system, and the magnetic field oriented two-phase rotation  $M$ - $T$  coordinate system. The relationship between several coordinate systems is shown in Figure 1.  $\theta$  is the flux linkage angle, and the included angle between axis  $M$  and axis  $d$   $\delta$  is called the load angle. The angle between axis  $\alpha$  and axis  $d$   $\gamma$  is the rotor position angle.

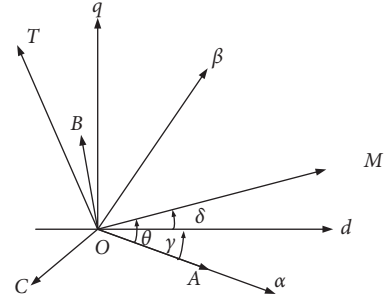


FIGURE 1: Reference coordinates of the synchronous motor.

The rotor axis of EESM is defined as the  $d$ -axis, and the motor model established with the  $d$ - $q$  axis as the coordinate system is in the  $d$ - $q$  coordinate system, which transforms the relevant variables of the stator of the motor into the rotor position orientation. To obtain a better control effect, the direction of air-gap flux is selected as  $M$ -axis, and the  $M$ - $T$  coordinate system is established.

- (1) The equation of flux in the  $M$ - $T$  coordinate system is

$$[\psi]_{mt} = [L]_{mt} [I]_{mt}, \quad (1)$$

where flux matrix and current matrix in  $M$ - $T$  coordinate system are, respectively:  $[\psi]_{mt} = [\psi_{sm} \ \psi_{st} \ \psi_f \ 0 \ 0]^T$  and  $[I]_{mt} = [i_{sm} \ i_{st} \ i_f \ 0 \ 0]^T$ .

Then the inductance coefficient matrix is

$$[L]_{mt} = \begin{bmatrix} L_{sl} + L_{am} & -L_{ao} & L_{ad} \cos \delta & L_{ad} \cos \delta & L_{aq} \sin \delta \\ -L_{ao} & L_{sl} + L_{at} & -L_{ad} \sin \delta & -L_{ad} \sin \delta & -L_{aq} \cos \delta \\ L_{ad} \cos \delta & -L_{ad} \sin \delta & L_f & L_{ad} & 0 \\ L_{ad} \cos \delta & -L_{ad} \sin \delta & L_{ad} & L_{Dd} & 0 \\ L_{aq} \sin \delta & -L_{aq} \cos \delta & 0 & 0 & L_{Dq} \end{bmatrix}, \quad (2)$$

where  $L_{am} = 1/2(L_{ad} + L_{aq}) + 1/2(L_{ad} - L_{aq})\cos 2\delta$ ,  $L_{at} = 1/2(L_{ad} + L_{aq}) - 1/2(L_{ad} - L_{aq})\cos 2\delta$ , and  $L_{ao} = 1/2(L_{ad} - L_{aq})\sin 2\delta$ .

- (2) The voltage equation of the motor  $M$ - $T$  axis is

$$[U]_{mt} = [R]_{mt} [I]_{mt} + p[\psi]_{mt} + [Y][\psi]_{mt}, \quad (3)$$

where the voltage matrix, resistance matrix, and matrix  $[Y]$  are described, respectively,  $[U]_{mt} = [u_{sm} \ u_{st} \ u_f \ 0 \ 0]^T$ ,  $[R]_{mt} = \text{diag} [R_s \ R_s \ R_f \ R_{Dd} \ R_{Dq}]^T$ , and  $[Y]$

$$= \begin{bmatrix} 0 & -(\omega_r + \omega_\delta) & 0 & 0 & 0 \\ \omega_r + \omega_\delta & 0 & 0 & 0 & 0 \\ 0 & 0 & 0 & 0 & 0 \\ 0 & 0 & 0 & 0 & 0 \\ 0 & 0 & 0 & 0 & 0 \end{bmatrix}.$$

- (3) Mathematical expression of torque is

$$T_e = p_m (\psi_{sm} i_{st} - \psi_{st} i_{sm}), \quad (4)$$

where  $p_m$  is the pole logarithm of EESM.

- (4) The relationships between electromechanical magnetic torque, load torque, and speed are as follows:

$$T_e - T_L = J \frac{d\omega_r}{dt}. \quad (5)$$

## 3. Speed Sensorless Control Based on Initial Rotor Position Detection for EESM

**3.1. Principle of Initial Rotor Position Detection.** The excitation windings of EESM can be regarded as a transformer with a variable coupling coefficient, which is related to the position of the rotor. The excitation windings can be

regarded as the primary side of the transformer, and the stator windings of each phase can be regarded as a secondary side of the transformer. The ratio between the primary side and the secondary side is related to the position of the rotor.

The principle of the rotor high-frequency signal injection method is to short-circuit the three-phase windings of the stator of an electrically excited synchronous motor, through which alternating current is passed, and the alternating magnetic field will generate induced electromotive force in the three-phase stator windings. The rotor position angle can be indirectly determined by judging the amplitude and phase of the electromotive force of each phase. Assume that the current flowing into the excitation winding is

$$i_f = I_{fm} \sin(\omega_f t), \quad (6)$$

where  $I_{fm}$  is the amplitude of the excitation current and  $\omega_f$  is the angular frequency of the excitation current.

When the stator side is short-connected, the component of the stator current in the  $d$ - $q$  coordinate system is

$$\begin{cases} i_d = -\frac{M_{sff}}{L_{dd}} i_f, \\ i_q = 0, \end{cases} \quad (7)$$

where  $M_{sff} = M_{sf} - M_{fD}M_{sD}/L_D$  and  $L_{dd} = L_d - 1.5M_{sD}^2/L_D$ .

As shown in (7), when the rotor current is constant, the direct axis component of the stator side induced current is related to the rotor position, so the initial position angle of the rotor can be derived directly by analyzing the position of the current vector. According to the coordinate system relationship shown in Figure 1, the stator current in the  $d$ - $q$  coordinate system is transformed to the  $\alpha$ - $\beta$  coordinate system, and the transformation relationship is

$$\begin{cases} i_\alpha = -\frac{M_{sff}}{L_{dd}} i_f \cos \gamma, \\ i_\beta = -\frac{M_{sff}}{L_{dd}} i_f \sin \gamma. \end{cases} \quad (8)$$

Multiply both sides of equation (8) by the excitation current  $i_f$  as follows:

$$\begin{cases} i_\alpha i_f = -\frac{M_{sff}}{L_{dd}} i_f^2 \cos \gamma = -\frac{M_{sff}}{2L_{dd}} i_f^2 \cos \gamma + \frac{M_{sff}}{2L_{dd}} i_f^2 \cos \gamma \cos(2\omega t), \\ i_\beta i_f = -\frac{M_{sff}}{L_{dd}} i_f^2 \sin \gamma = -\frac{M_{sff}}{2L_{dd}} i_f^2 \sin \gamma + \frac{M_{sff}}{2L_{dd}} i_f^2 \sin \gamma \cos(2\omega t). \end{cases} \quad (9)$$

The two equations in equation (9) are composed of two parts. The first part is the DC component related to the rotor's initial position angle, and the second part is the AC component related to the rotor side excitation current frequency. The low-pass filter can be used to filter out AC components and extract DC components for analysis. The cut-off frequency of the low-pass filter used in this paper is  $0.2\omega$ . After filtering by a low-pass filter, the following equation can be obtained:

$$\begin{cases} LPF(i_\alpha i_f) = -\frac{M_{sff}}{2L_{dd}} i_f^2 \cos \gamma, \\ LPF(i_\beta i_f) = -\frac{M_{sff}}{2L_{dd}} i_f^2 \sin \gamma. \end{cases} \quad (10)$$

The initial position angle of the rotor can be easily requested according to equation (10). The principle of the

initial position angle of the rotor of the open ring method is shown in Figure 2. In this paper, the stator current value of the stator current and the rotor excitation current value are given by the  $\alpha$ - $\beta$  coordinate system, and the calculation results are obtained by the low-pass filter. Then the DC component of the initial position angle of the rotor is obtained. Finally, the sine and cosine value of the initial rotor position angle is obtained by the operation of the open square and the division method, and the size of the initial angle of the rotor is determined.

It is well known that the design of the filter needs to be selected for the parameters of the various parameters. Therefore, to simplify the calculation and improve the efficiency, the sliding Fourier transition (SDFT) has been proposed to extract the rotor position component in this paper.

The discrete Fourier transform of the finite length sequence  $x(n)$  can be expressed as follows:

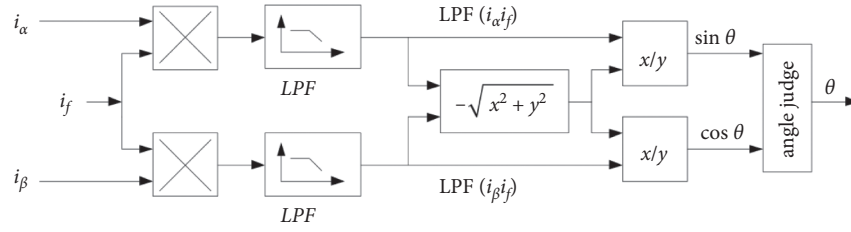


FIGURE 2: The principle of the initial rotor position angle of the rotor of the open ring method.

$$X(k) = DFT[x(n)] = x(0) + x(1)e^{-j\frac{2\pi k}{N}} + x(2)e^{-j\frac{2\pi k \times 2}{N}} + \dots + x(N-1)e^{-j\frac{2\pi k \times (N-1)}{N}}, \quad (11)$$

where  $N$  is the length of the data.

As shown in Figure 3, the data graph of SDFT is presented.  $x(0)$  is the first group of data collected, and  $x(1)$  is the second group of data collected.

The discrete Fourier transform of the two sets of data collected can be obtained as follows:

$$\begin{cases} X_0(k) = x(0) + x(1)e^{-j\frac{2\pi k}{N}} + x(2)e^{-j\frac{2\pi k \times 2}{N}} + \dots + x(N-1)e^{-j\frac{2\pi k \times (N-1)}{N}}, \\ X_1(k) = x(1) + x(2)e^{-j\frac{2\pi k}{N}} + x(3)e^{-j\frac{2\pi k \times 2}{N}} + \dots + x(N)e^{-j\frac{2\pi k \times (N-1)}{N}}. \end{cases} \quad (12)$$

From equation (12), the relation between two sets of discrete Fourier transforms and the expression of SDFT can be obtained as follows:

$$X_1(k) = [X_0(k) - x(0) + x(N)]e^{j\frac{2\pi k}{N}}. \quad (13)$$

It can be seen from equation (13) that the Fourier transform the expression of the new sampling sequence can be obtained through the data of the sampling point at the previous moment, which saves a lot of operation time and improves the processing efficiency. The specific process is as follows: by subtracting the DC term  $x(0)$  in the sampling sequence from the Fourier transform formula of the sampling point data  $X_0(k)$  at the previous time and then by adding  $x(N)$  to the result obtained by phase shift processing, the Fourier transform of the new sampling sequence  $X_1(k)$  can be obtained. The whole process only requires simple addition and subtraction and an auxiliary multiplication for the Fourier transform of the sampling sequence at the previous moment. This data processing method is much more efficient than FFT and is very suitable for digital processors to process high-frequency signals. Figure 4 shows the principle of rotor initial position angle detection using SDFT to extract position components.

**3.2. Speed Sensorless Control Principle of Rotor Signal Injection Method.** EESM speed regulation system is a high-order, strong coupling, nonlinear, multivariable complex system; different from permanent magnet synchronous motor

rotor for permanent magnet structure, EESM rotor is powered by the external power supply and provides rotor magnetic field. When the signal injection method is used, the rotor position can be detected by injecting a high-frequency signal at the rotor side, considering the asymmetry of the structure of the salient pole electroexcitation synchronous motor and the structure of the rotor external excitation.

Because there are excitation windings on the rotor side of the electrically excited synchronous motor, high-frequency signal can be injected into the rotor side to detect the rotor position. As shown in Figure 5, the fixed rotor of EESM can be simplified into the coupling transformer shown in the figure. After the high-frequency current signal is injected into the rotor side, the rotor position can be determined by detecting the high-frequency current signal induced by the stator side.

Assume that the current flowing into the rotor is

$$\begin{aligned} i_f &= I_f + I_h \sin(\omega_h t + \varphi) \\ &= i_{f-} + i_{f\sim}, \end{aligned} \quad (14)$$

where  $i_{f-}$  is the DC component of rotor excitation current,  $i_{f\sim}$  is the AC component of rotor excitation current,  $I_f$  is the magnitude of the DC component,  $I_h$  is the amplitude of high-frequency AC component of rotor excitation current,  $\omega_h$  is the angular frequency of the high-frequency AC component of the rotor excitation current, and  $\varphi$  is the phase angle of high-frequency AC component of rotor excitation current.

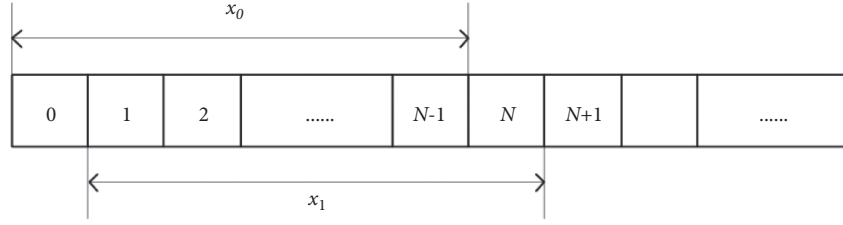


FIGURE 3: The data graph of SDFT.

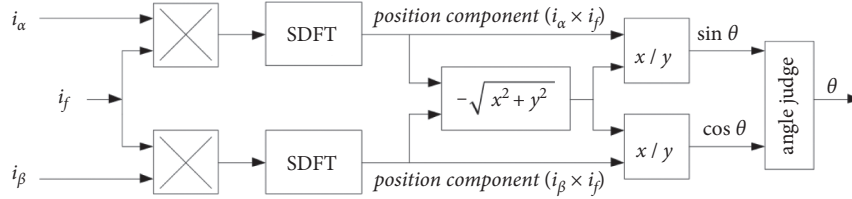


FIGURE 4: The principle of rotor initial position angle detection using SDFT to extract position components.

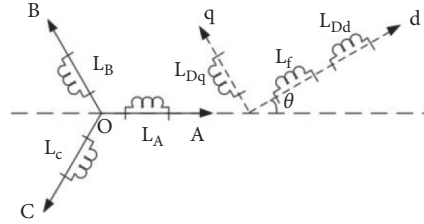


FIGURE 5: Simplified stator and rotor structure of EESM.

Due to the existence of high-frequency signal in the excitation current, when the current through the rotor, the corresponding high-frequency quantity will be induced on the stator side of the motor. Set the corresponding high-frequency quantity induced by the stator  $ABC$  as  $i_{a\sim}$ ,  $i_{b\sim}$ , and  $i_{c\sim}$ ; the following expressions can be obtained according to the fixed rotor and the angle between the fixed rotors:

$$\begin{cases} i_{a\sim} = i_{f\sim} \cos \theta, \\ i_{b\sim} = i_{f\sim} \cos\left(\theta - \frac{2\pi}{3}\right), \\ i_{c\sim} = i_{f\sim} \cos\left(\theta + \frac{2\pi}{3}\right). \end{cases} \quad (15)$$

Substitute high-frequency current  $i_{f\sim}$  into equation (15) to obtain the following equation:

$$\begin{cases} i_{f\sim} = I_h \sin(\omega_h t + \varphi), \\ i_{a\sim} = I_h \sin(\omega_h t + \varphi) \cos \theta, \\ i_{b\sim} = I_h \sin(\omega_h t + \varphi) \cos\left(\theta - \frac{2\pi}{3}\right), \\ i_{c\sim} = I_h \sin(\omega_h t + \varphi) \cos\left(\theta + \frac{2\pi}{3}\right). \end{cases} \quad (16)$$

Through Clark transformation,  $ABC$  coordinate system is transformed into the  $\alpha\beta$  coordinate system as follows:

$$\begin{aligned} \begin{bmatrix} i_{\alpha\sim} \\ i_{\beta\sim} \end{bmatrix} &= \sqrt{\frac{2}{3}} \begin{bmatrix} 1 & \frac{1}{2} & \frac{1}{2} \\ 0 & \frac{\sqrt{3}}{2} & -\frac{\sqrt{3}}{2} \end{bmatrix} \begin{bmatrix} i_a \\ i_b \\ i_c \end{bmatrix} \\ &= \sqrt{\frac{3}{2}} I_h \sin(\omega_h t + \varphi) \begin{bmatrix} \cos \theta \\ \sin \theta \end{bmatrix}. \end{aligned} \quad (17)$$

To obtain the rotor position, equation (17) is further processed. Multiplying equation (17) by  $\sin \omega_h t$  results in the following formula:

$$\begin{aligned} \sin \omega_h t \begin{bmatrix} i_{\alpha\sim} \\ i_{\beta\sim} \end{bmatrix} &= \sqrt{\frac{3}{2}} I_h \sin(\omega_h t + \varphi) \sin \omega_h t \begin{bmatrix} \cos \theta \\ \sin \theta \end{bmatrix} \\ &= \frac{1}{2} \sqrt{\frac{3}{2}} I_h \begin{bmatrix} \cos \varphi \cos \theta - \cos(2\omega_h t + \varphi) \cos \theta \\ \cos \varphi \sin \theta - \cos(2\omega_h t + \varphi) \sin \theta \end{bmatrix}. \end{aligned} \quad (18)$$

As shown in equation (18), the result contains constant term and high-frequency term. After the high-frequency part is filtered out by a low-pass filter, the constant term containing rotor position information can be obtained, expressed as follows:

$$\begin{aligned} \begin{bmatrix} LPF(i_{\alpha\sim} \sin \omega_h t) \\ LPF(i_{\beta\sim} \sin \omega_h t) \end{bmatrix} &= \frac{1}{2} \sqrt{\frac{3}{2}} I_h \cos \varphi \begin{bmatrix} \cos \theta \\ \sin \theta \end{bmatrix} \\ &= K_h \begin{bmatrix} \cos \theta \\ \sin \theta \end{bmatrix}. \end{aligned} \quad (19)$$

where  $K_h = 1/2 \sqrt{3/2} I_h \cos \varphi$ .

Through PLL processing on equation (19), the rotor position can be extracted, and the block diagram is shown in Figure 6.

**3.3. Influence of Damping Winding on Speed Sensorless Method of High-Frequency Signal Injection.** According to the mathematical model of EESM in Section 2, there are damping windings in the  $d$ - $q$  axis of EESM, and the existence

of damping windings also has a corresponding influence on the high-frequency signals induced from the stator. Since the rotor windings are injected with high-frequency components, the corresponding high-frequency components will also be induced in the damping windings of the  $d$ -axis, and since the  $q$ -axis is perpendicular to the  $d$ -axis, the damping windings on the  $q$ -axis will not induce the high-frequency components.

The high-frequency current component induced from the damping winding of the  $d$ -axis is set as follows:

$$i_{Dd\sim} = I_{Dd} \sin(\omega_h t + \varphi_{Dd}), \quad (20)$$

where  $I_{Dd}$  is the amplitude of the high-frequency component of the damping winding of the  $d$ -axis and  $\varphi_{Dd}$  is the phase angle of the high-frequency component of the damping winding of the  $d$ -axis. Then the induced current in the stator winding is

$$\begin{aligned} \begin{bmatrix} i_a \\ i_{b\sim} \\ i_c \end{bmatrix} &= \begin{bmatrix} (i_{f\sim} + i_{Dd\sim}) \cos \theta \\ (i_f + i_{Dd\sim}) \cos\left(\theta - \frac{2\pi}{3}\right) \\ (i_{f\sim} + i_{Dd\sim}) \cos\left(\theta + \frac{2\pi}{3}\right) \end{bmatrix} \\ &= \begin{bmatrix} [I_h \sin(\omega_h t + \varphi) + I_{Ddh} \sin(\omega_h t + \varphi_{Dd})] \cos \theta \\ [I_h \sin(\omega_h t + \varphi) + I_{Ddh} \sin(\omega_h t + \varphi_{Dd})] \cos\left(\theta - \frac{2\pi}{3}\right) \\ [I_h \sin(\omega_h t + \varphi) + I_{Ddh} \sin(\omega_h t + \varphi_{Dd})] \cos\left(\theta + \frac{2\pi}{3}\right) \end{bmatrix}. \end{aligned} \quad (21)$$

According to the signal processing method in Section 3.2, equation (21) is transformed from  $ABC$  coordinate

system to  $\alpha$ - $\beta$  coordinate system, and it can be expressed as follows:

$$\begin{bmatrix} i_{\alpha\sim} \\ i_{\beta\sim} \end{bmatrix} = \sqrt{\frac{3}{2}} I_h \sin(\omega_h t + \varphi) \begin{bmatrix} \cos \theta \\ \sin \theta \end{bmatrix} + \sqrt{\frac{3}{2}} I_{Ddh} \sin(\omega_h t + \varphi_{Dd}) \begin{bmatrix} \cos \theta \\ \sin \theta \end{bmatrix}. \quad (22)$$

Then multiply equation (22) by  $\sin \omega_h t$ , and the following equation can be obtained through operation and simplification:

$$\sin \omega_h t \begin{bmatrix} i_{\alpha\sim} \\ i_{\beta\sim} \end{bmatrix} = \frac{1}{2} \sqrt{\frac{3}{2}} [(I_h \cos \varphi + I_{Ddh} \cos \varphi_{Dd}) - I_h \cos(2\omega_h t + \varphi) - I_{Ddh} \cos(2\omega_h t + \varphi_{Dd})] \begin{bmatrix} \cos \theta \\ \sin \theta \end{bmatrix}. \quad (23)$$



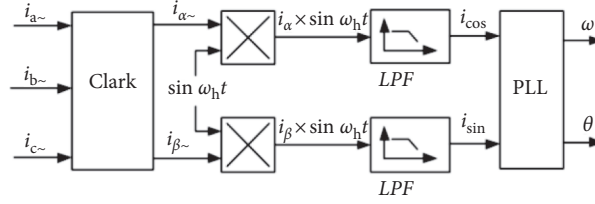


FIGURE 6: Block diagram of rotor position detection by high frequency injection method.

As can be seen from the above equation, the last two terms of the equation are high-frequency terms containing twice the angular frequency of the rotor winding injection

current, and the DC component can be extracted through the low-pass filter. The formula after passing the low-pass filter is as follows:

$$\begin{bmatrix} LPF(\sin \omega_h t \times i_{\alpha\sim}) \\ LPF(\sin \omega_h t \times i_{\beta\sim}) \end{bmatrix} = \frac{1}{2} \sqrt{\frac{3}{2}} (I_h \cos \varphi + I_{Ddh} \cos \varphi_{Dd}) \begin{bmatrix} \cos \theta \\ \sin \theta \end{bmatrix}. \quad (24)$$

By comparing equations (24) and (19), it can be known that after considering the damping windings, the quantity containing the position signal through the low-pass filter is only different in coefficient. Therefore, the existence of damping windings does not affect the detection results.

**3.4. Speed Sensorless System Based on High-Frequency Signal Injection.** The flux equation of EESM is

$$\begin{cases} \psi_{sd} = L_d i_{sd} + L_{ad} i_f + L_{ad} i_{Dd}, \\ \psi_{sq} = L_d i_{sq} + L_{ad} i_{Dq}. \end{cases} \quad (25)$$

Under the condition of ignoring the influence of damping windings, the high-frequency flux equation of EESM can be written as follows:

$$\begin{cases} \psi_{sd\sim} = L_d i_{sd\sim} + L_{ad} i_{f\sim}, \\ \psi_{sq\sim} = L_d i_{sq\sim}. \end{cases} \quad (26)$$

When the high-frequency component is injected, the  $d$ - $q$  axis flux of EESM can be expressed as follows:

$$\begin{cases} \psi_{sd} = \psi_{sd-} + \psi_{sd\sim}, \\ \psi_{sq} = \psi_{sq-} + \psi_{sq\sim}. \end{cases} \quad (27)$$

where  $\psi_{sd-}$  and  $\psi_{sq-}$  is the DC component of the  $d$ - $q$  axis of flux linkage and  $\psi_{sd\sim}$  and  $\psi_{sq\sim}$  is the high frequency component of the  $d$ - $q$  axis of flux.

The following equation can be obtained from equation (26):

$$i_{sd\sim} = \frac{\psi_{sd\sim}}{L_d} - \frac{L_{ad}}{L_d} i_{f\sim}. \quad (28)$$

To make the rotor position information completely in the  $d$ -axis component of the motor stator current, it is necessary to control the high-frequency component of the  $d$ -axis of the motor flux to be 0. Due to vector control, the flux of EESM is constant, so the equation of flux amplitude can be written as follows:

$$\begin{aligned} |\psi| &= \sqrt{(\psi_{sd-} + \psi_{sd\sim})^2 + (\psi_{sq-} + \psi_{sq\sim})^2} \\ &= C. \end{aligned} \quad (29)$$

It can be seen from equation (29) that  $\psi_{sd\sim} = 0$  is realized by controlling  $\psi_{sq\sim} = 0$ . According to equation (26), the high-frequency  $q$ -axis component of flux is proportional to the high-frequency  $q$ -axis component of stator current, so the above control theory can be realized when  $i_{sq\sim} = 0$ . Figure 7 shows the relationship between the high-frequency components of the flux linkage.

In the vector control system of EESM, the outer speed loop passes through the PI regulator, and the output is given  $T_e^*$  for electromagnetic torque. The control  $i_{sq\sim} = 0$  can be realized by compensating at  $T_e^*$ . The electromagnetic torque equation of EESM is

$$T_e = \frac{1}{2} n_p [(L_d - L_q) i_{sd} i_{sq} + L_{ad} i_{sq} i_f + L_{ad} i_{sq} i_{Dd} - L_{aq} i_{sd} i_{Dq}]. \quad (30)$$

Since the damping windings do not affect the judgment of rotor position, the damping windings are ignored, and the electromagnetic torque equation can be written as follows:

$$T_e = \frac{1}{2} n_p [(L_d - L_q) i_{sd} i_{sq} + L_{ad} i_{sq} i_f]. \quad (31)$$

When  $i_{sq\sim} = 0$ , the expressions of  $i_{sd}$  and  $i_{sq}$  are described as follows:

$$\begin{cases} i_{sd} = i_{sd-} + i_{sd\sim} = i_{sd-} - \frac{L_{ad}}{L_d} i_{f\sim} \\ i_{sq} = i_{sq-} + i_{sq\sim} = i_{sq-} \\ i_f = I_f + I_h \sin(\omega t + \varphi) \end{cases} \quad (32)$$

Then the electromagnetic torque equation can be written as follows:



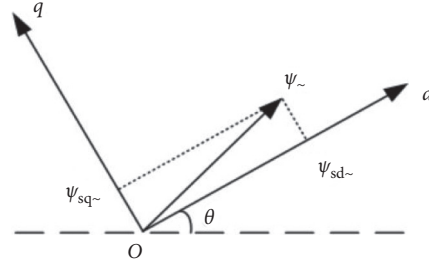


FIGURE 7: High-frequency component of flux linkage.

$$\begin{aligned}
 T_e &= \frac{1}{2} n_p \left\{ (L_d - L_q) \left[ i_{sd-} - \frac{L_{ad}}{L_d} I_h \sin(\omega t + \varphi) \right] i_{sq-} + L_{ad} i_{sq-} \left[ I_f + I_h \sin(\omega t + \varphi) \right] \right\} \\
 &= \frac{1}{2} n_p \left[ (L_d - L_q) i_{sd-} + L_{ad} I_f \right] i_{sq-} + \frac{1}{2} n_p \left[ (L_d - L_q) \frac{L_{ad}}{L_d} I_h + L_{ad} I_h \right] \sin(\omega t + \varphi) i_{sq-} \\
 &= T_e^* + \frac{1}{2} n_p \left[ (L_d - L_q) \frac{L_{ad}}{L_d} I_h + L_{ad} I_h \right] \sin(\omega t + \varphi) i_{sq-}.
 \end{aligned} \tag{33}$$

It can be seen from equation (33) that because of the original output of the speed loop, additional high-frequency quantity needs to be injected into current loop, expressed as follows:

$$T_{e\sim} = \frac{1}{2} n_p \left[ (L_d - L_q) \frac{L_{ad}}{L_d} I_h + L_{ad} I_h \right] \sin(\omega t + \varphi) i_{sq-}. \tag{34}$$

The control block diagram of the speed sensorless vector control system of EESM using this method is shown in Figure 8. In the figure, torque high-frequency feed quantification is introduced into the speed ring output as the compensation of high frequency signal, and speed feedback is estimated by the speed sensorless method.

### 3.5. Design of Phase-Locked Loop to Extract Rotor Position.

After eliminating the influence of the  $q$ -axis, the phase-locked loop (PLL) is designed to obtain the motor position and speed. According to the results obtained from Section 3.2, Park transform is used as a phase detector, and the block diagram of the designed PLL is shown in Figure 9.

The expression of Park transform for the signal after the low-pass filter is as follows:

$$\begin{aligned}
 \begin{bmatrix} i_{d\theta} \\ i_{q\theta} \end{bmatrix} &= K_h \begin{bmatrix} \cos \hat{\theta} & \sin \hat{\theta} \\ -\sin \hat{\theta} & \cos \hat{\theta} \end{bmatrix} \begin{bmatrix} \cos \theta \\ \sin \theta \end{bmatrix} \\
 &= \begin{bmatrix} K_h \cos \hat{\theta} \cos \theta + K_h \sin \hat{\theta} \sin \theta \\ -K_h \sin \hat{\theta} \cos \theta + K_h \cos \hat{\theta} \sin \theta \end{bmatrix},
 \end{aligned} \tag{35}$$

where  $i_{q\theta} = -K_h \sin \hat{\theta} \cos \theta + K_h \cos \hat{\theta} \sin \theta = K_h \sin(\theta - \hat{\theta})$ .

When the difference between  $\theta$  and  $\hat{\theta}$  is very small,  $\sin(\theta - \hat{\theta}) \approx \theta - \hat{\theta}$ , then

$$i_{q\theta} = K_h (\theta - \hat{\theta}). \tag{36}$$

Set the expression of PLL PI function as  $k_{\theta p} + k_{\theta i}/s$ ; the transfer function between the observed value and the actual value can be derived as follows:

$$\begin{aligned}
 G(s) &= \frac{\hat{\theta}}{\theta} \\
 &= \frac{\hat{\omega}}{\omega} \\
 &= \frac{K_h k_{\theta p} s + K_h k_{\theta i}}{s^2 + K_h k_{\theta p} s + K_h k_{\theta i}}.
 \end{aligned} \tag{37}$$

By substituting the transfer function into the design of the speed ring, a block diagram of the speed ring without a speed sensor can be obtained as shown in Figure 10.

According to Figure 10, the speed closed-loop transfer function is

$$\frac{\omega}{\omega^*} = \frac{K_{pn} s^3 + (K_h k_{\theta p} K_{pn} + K_{in}) s^2 + (K_h k_{\theta i} K_{pn} + K_h k_{\theta p}) s + K_h k_{\theta i} K_{in}}{\left[ J T_{eq,i} s^5 + (J T_{eq,i} K_h k_{\theta p} + J) s^4 + (J T_{eq,i} K_h k_{\theta i} + J K_h k_{\theta p}) s^3 \right.} \tag{38}$$

$$\left. + (J K_h k_{\theta i} + K_h k_{\theta p} K_{pn}) s^2 + (K_h k_{\theta i} K_{pn} + K_h k_{\theta p} K_{in}) s + K_h k_{\theta i} K_{in} \right]}.$$

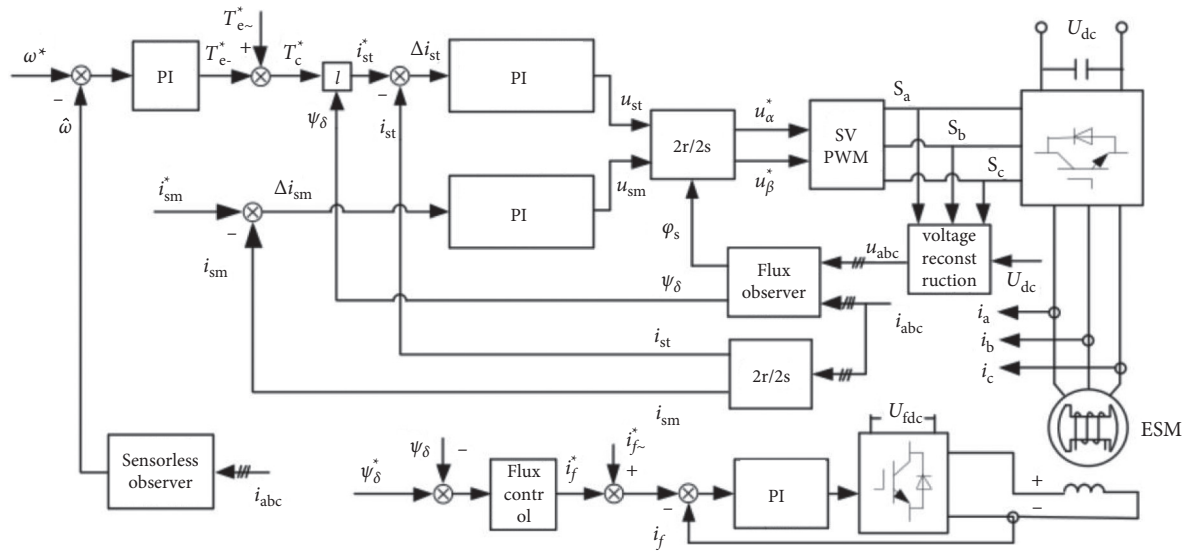


FIGURE 8: Speed sensorless vector control system of EESM.

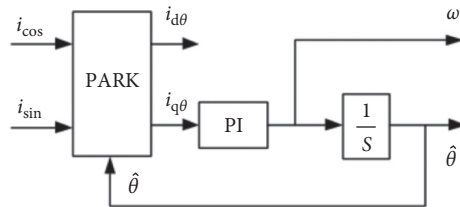


FIGURE 9: Phase-locked loop block diagram in speed sensorless control.

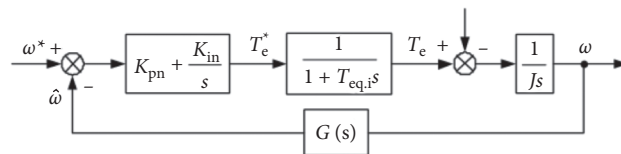


FIGURE 10: Speed sensorless closed-loop system diagram.

### 4. Simulated Analysis

MATLAB/Simulink was used to simulate the proposed speed sensorless control method based on initial rotor position detection and the conventional speed sensorless method, and the motor parameters are shown in Table 1.

**4.1. Initial Rotor Position Detection Simulation.** To verify the efficiency of the proposed initial rotor position detection method, comparisons between the traditional voltage integration method and the SDFT method have been conducted, and the simulation waveform is described in Figure 11.

Figure 11 shows the simulation waveform when the rotor's initial position angle is 60°. In Figure 11, red is the reference line of 60°, and blue is the waveform of the rotor's initial position angle measured by simulation. It can be seen from Figure 11(a) that the traditional voltage integration method not only has zero drift at the beginning of measurement but also has more and more DC bias due to

integration as time increases. It can be seen from Figure 11(b) that the measurement of the initial position angle of the motor rotor by using the rotor signal injection method is very accurate and will not be offset due to time limitations.

To verify that the method in this paper can detect the initial position value and start the EESM at any position, a simulation experiment is carried out every 10°, and the results measured in the simulation experiment are sorted out from the theoretical perspective, as shown in Table 2.

With the theoretical angle value as the horizontal axis and the simulated detection value as the vertical axis, the fitting degree diagram between the rotor position obtained by the initial position detection simulation method and the theoretical rotor angle can be compared, as shown in Figure 12.

As can be seen from Figure 12, the rotor at any position can be obtained through the initial position detection method, and there is good linearity between the tested value and the theoretical value, so the excitation synchronous motor can be started at any position.

TABLE 1: EESM parameters.

Specification	Value	Specification	Value
Power (kW)	8	$q$ -axis armature reaction inductance (mH)	51.8
DC link voltage (V)	380	Stator winding leakage inductance (mH)	4.5
Rated speed (r/min)	1500	Rotor winding leakage inductance (mH)	11.3
Number of pole pairs	2	$d$ -axis damping winding resistance ( $\Omega$ )	3.14
Stator resistance ( $\Omega$ )	1.62	$q$ -axis damping winding resistance ( $\Omega$ )	4.77
Rotor resistance ( $\Omega$ )	1.2	$d$ -axis damping winding leakage inductance (mH)	7.33
$d$ -axis armature reaction inductance (mH)	108.6	$q$ -axis damping winding leakage inductance (mH)	10.15

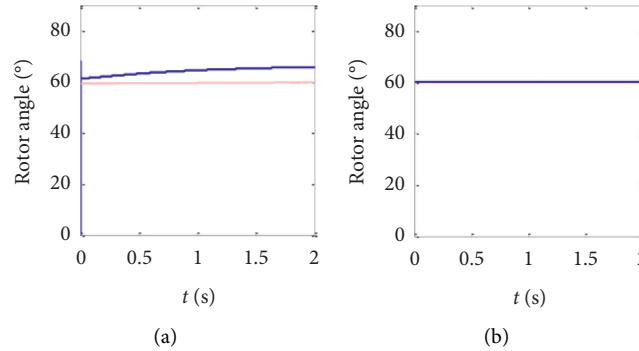


FIGURE 11: Simulation waveform of initial rotor position detection. (a) Traditional voltage integration method and (b) improved signal injection method.

TABLE 2: Initial position detection table of EESM.

Theoretical value (°)	Detection value (°)	Theoretical value (°)	Detection value (°)	Theoretical value (°)	Detection value (°)	Theoretical value (°)	Detection value (°)
0	0.95	90	90.3	180	181.1	270	269.1
10	10.6	100	99.3	190	191.6	280	281.5
20	19.8	110	110.9	200	202.3	290	290.3
30	30.2	120	120.5	210	209.2	300	300.2
40	40.5	130	131.2	220	221.4	310	311.1
50	50.6	140	140.7	230	231.6	320	320.6
60	61.3	150	152.1	240	241.9	330	330.5
70	71.5	160	162.5	250	251.3	340	341.9
80	80.6	170	170.8	260	260.2	350	350.7

4.2. *Speed Sensorless Control Simulation of EESM.* The speed sensorless control method of EESM based on the rotor high-frequency signal injection method is simulated by MATLAB/Simulink. The simulation procedure is given as follows: (1) the simulation speed is given as a step signal with a sudden change of 0.5 s to the rated speed of 1,500 rpm; (2) injecting 1,000 Hz high-frequency component into the rotor side of EESM; and (3) collecting the stator current and obtaining the high-frequency component of stator current through the band-pass filter. The local amplification waveform of high-frequency component of stator current of EESM is shown as Figure 13.

The speed sensorless principle described in Section 3.1 is used to process the high-frequency component of stator current, and the calculation principle block diagram of speed and rotor position angle is shown in Figure 14.

The speed sensorless simulation is built according to Figure 14, and the speed waveform is obtained, as shown in Figure 15. When the motor speed is 0.5 s, it suddenly changes

from 0 rpm to a rated speed of 1,500 rpm. In Figure 15(a), the blue waveform is the speed estimation waveform, and the red waveform is the speed given waveform. Figure 15(b) is a partially enlarged view from the moment of a sudden change of speed to stable speed. It can be seen from the simulation waveform that when the speed of the step signal is given, the estimated speed value at the moment of a sudden change of speed will fluctuate. After a short fluctuation, the estimated speed value will fluctuate slightly near the given value, which can well estimate the motor speed.

The estimated waveform of rotor position angle is shown in Figure 16. In Figure 16(a), the blue waveform is the estimated rotor position angle waveform, and the red waveform is the actual rotor position angle waveform of the motor. It can be seen from the waveform that the error between the calculated value and the actual value is very small, which shows that the high-frequency signal injection method studied in this paper can accurately estimate the information of motor rotor position angle.

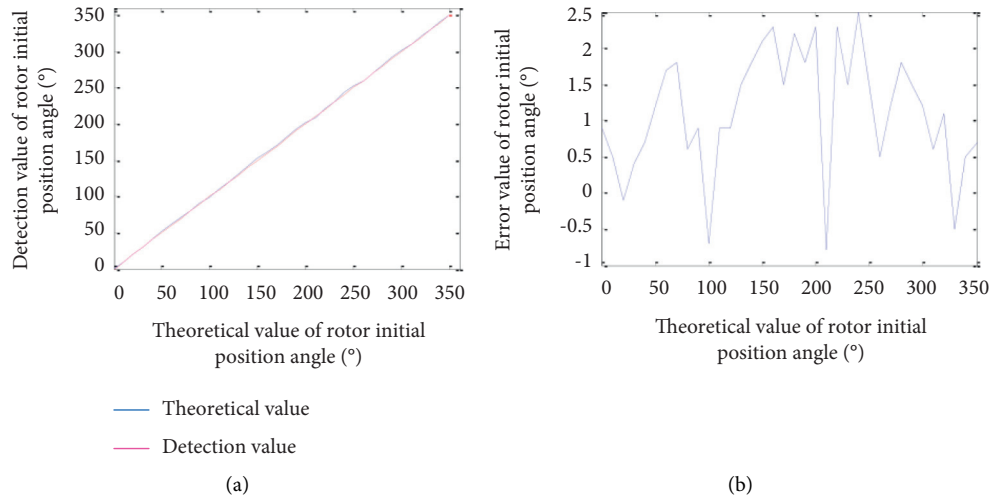


FIGURE 12: Relationship between the actual value and the detection value of rotor initial position angle. (a) Comparison between rotor initial position detection and actual value and (b) error diagram between rotor initial position detection and actual value.

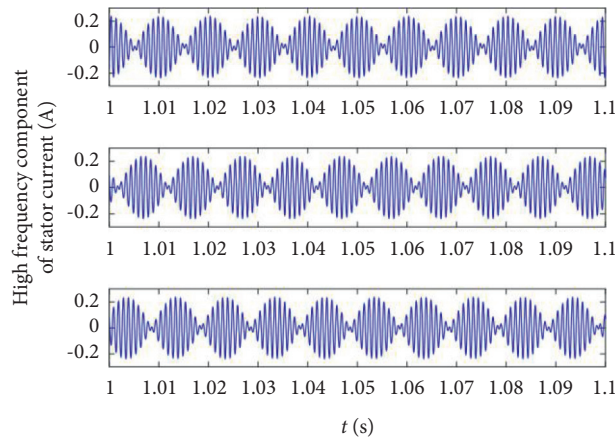


FIGURE 13: High-frequency component of stator current of EESM.

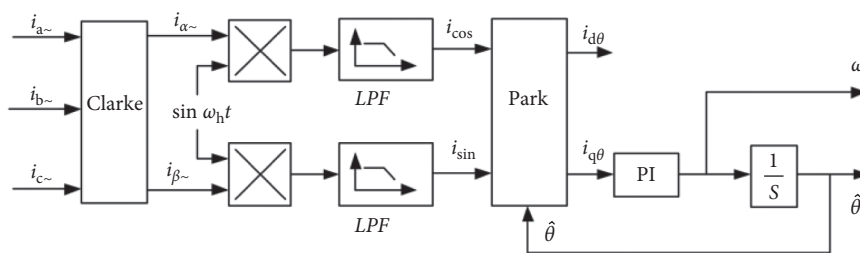


FIGURE 14: Speed sensorless signal processing schematic.

The speed sensorless control using high-frequency signal injection method of the EESM rotor is applied to the vector control system of EESM to estimate the motor speed and rotor position. In the simulation, the ramp signal is given when the speed is given at 0.5 s, the ramp signal finally reaches the rated speed of the motor 1,500 rpm, and the motor runs under a no-load state. The simulation waveform is shown in Figure 17.

Figure 17(a) shows the speed estimation waveform, the blue waveform in the figure is the actual speed waveform of

the motor, and the red waveform is the speed waveform estimated by the high-frequency signal injection method. Figure 17(b) shows the estimated waveform of rotor position angle; the blue waveform in the figure is the actual rotor position angle waveform of the motor; and the red waveform is the rotor position angle waveform estimated by the high-frequency signal injection method. Figure 17(c) shows the locally amplified waveform of rotor position angle estimation. It can be seen from the figure that the estimation of motor speed and rotor position angle is accurate, and there

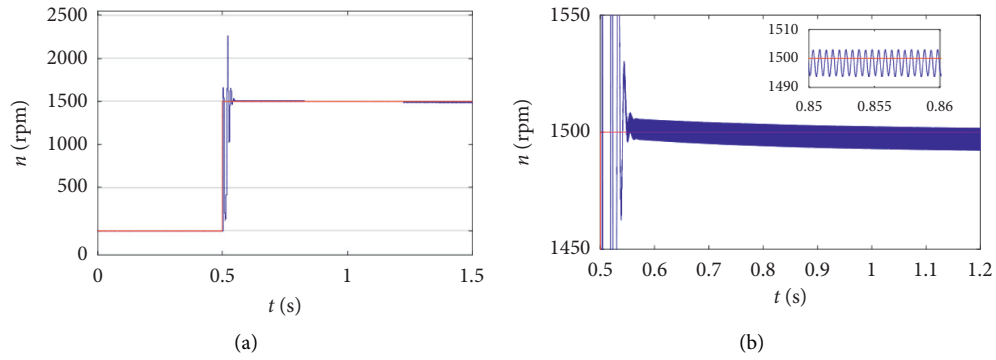


FIGURE 15: Speed estimation waveform of EESM by high-frequency signal injection method. (a) Comparison between speed estimation waveform and actual waveform and (b) enlarged drawing of comparison between speed estimation waveform and actual waveform.

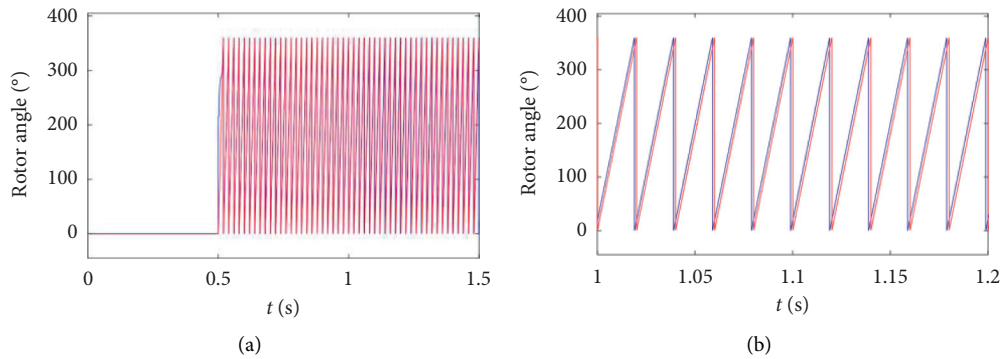


FIGURE 16: Rotor angle estimation waveform of EESM by high-frequency signal injection method. (a) Rotor actual and estimated position angle waveform and (b) partial enlarged view of rotor position angle.

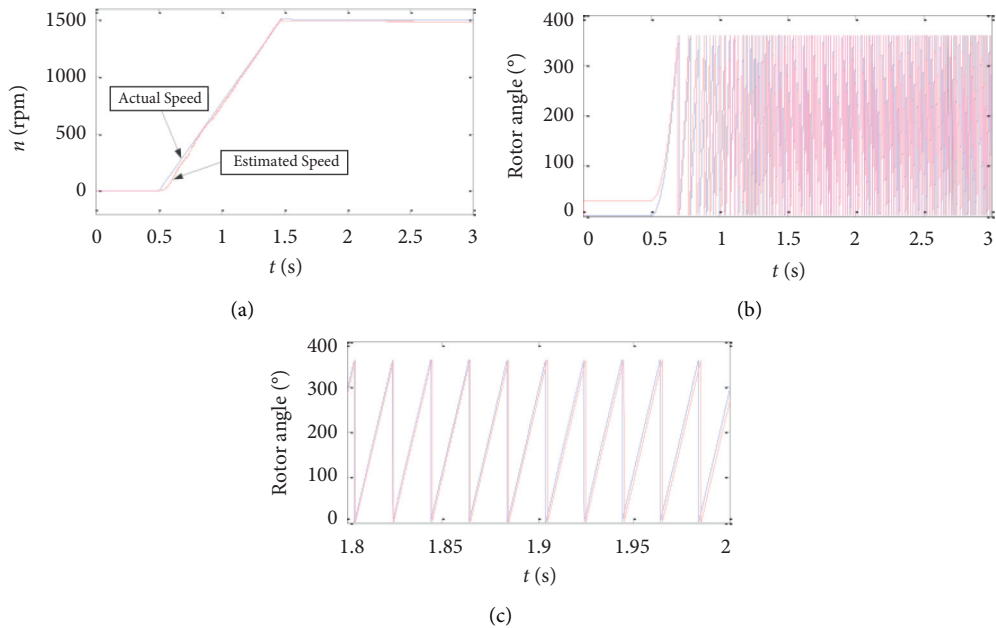


FIGURE 17: Simulation waveform of speed sensorless for vector control system of EESM. (a) Comparison between actual speed and estimated speed of motor, (b) comparison between actual angle and estimated angle of the rotor, and (c) enlarged view of comparison between actual angle and estimated angle of the rotor.

will be bias in the initial estimation of motor speed and rotor position angle, which is caused using an integrator in this high-frequency signal injection method.

## 5. Conclusions

In this paper, the measurement of motor initial position angle and the acquisition of motor rotor position information without speed sensor were studied. On the one hand, the rotor high-frequency signal injection method for detecting the initial position of the rotor can quickly and accurately obtain the rotor position angle. After introducing SDFI to improve the rotor high-frequency signal injection method, the DC component can be obtained directly, and the computational complexity can be reduced. On the other hand, the working principle of the rotor high-frequency signal injection method to obtain speed and rotor position angle was analyzed; the influence of damping winding on this method was analyzed; and the speed and rotor position angle observer of EESM was designed and realized.

Finally, after the above theoretical analysis and mathematical derivation, a series of simulations and experiments verify the feasibility and accuracy of the proposed method. As shown in simulation and experimental results, the proposed method can detect the initial rotor position precisely and accurately obtain the motor speed and rotor position signals under different operating conditions.

## Data Availability

The data used to support the findings of this study are included within the article.

## Conflicts of Interest

The authors declare that they have no conflicts of interest.

## Acknowledgments

This work was funded by the National Natural Science Foundation of China under Project 52002155.

## References

- [1] Y. Kali, M. Ayala, J. Rodas et al., "Current control of a six-phase induction machine drive based on discrete-time sliding mode with time delay estimation," *Energies*, vol. 12, no. 1, p. 170, 2019.
- [2] W. Hu, C. Ruan, H. Nian, and D. Sun, "Simplified modulation scheme for open-end winding PMSM system with common DC bus under open-phase fault based on circulating current suppression," *IEEE Transactions on Power Electronics*, vol. 35, pp. 10–14, 2019.
- [3] X. Ye, Z. Yang, and T. Zhang, "Modelling and performance analysis on a bearingless fixed-pole rotor induction motor," *IEEE Transactions on Applied Superconductivity*, vol. 13, pp. 259–266, 2019.
- [4] J. Karttunen, S. Kallio, J. Honkanen, P. Peltoniemi, and P. Silventoinen, "Partial current harmonic compensation in dual three-phase PMSMs considering the limited available voltage," *IEEE Transactions on Industrial Electronics*, vol. 64, no. 2, pp. 1038–1048, 2017.
- [5] W. E. Merrassi, A. Abounada, and M. Ramzi, "Switching losses analysis of a constructed solar DC-DC static boost converter," *Advances in Electrical and Electronic Engineering*, vol. 18, pp. 132–141, 2020.
- [6] J. Han, D. Kum, and Y. Park, "Synthesis of predictive equivalent consumption minimization strategy for hybrid electric vehicles based on closed-form solution of optimal equivalence factor," *IEEE Transactions on Vehicular Technology*, vol. 66, no. 7, pp. 5604–5616, 2017.
- [7] X. Sun, Z. Shi, J. Zhu, Y. Guo, and J. Zhu, "Multiobjective design optimization of an IPMSM for EVs based on fuzzy method and sequential taguchi method," *IEEE Transactions on Industrial Electronics*, vol. 68, no. 11, pp. 10592–10600, 2021.
- [8] Z. Yang, J. Ji, X. Sun, H. Zhu, and Q. Zhao, "Active disturbance rejection control for bearingless induction motor based on hyperbolic tangent tracking differentiator," *IEEE JEM SEL TOP P*, vol. 7, pp. 7456–7465, 2019.
- [9] J. Kou, Q. Gao, Z. Sha, Y. Teng, and D. Xu, "A rotor position detection method at high speed for electrically excited synchronous motor," in *Proceedings of the 22nd International Conference on Electrical Machines and Systems*, pp. 1–5, ICEMS), Harbin, China, August 2019.
- [10] W. E. Merrassi, A. Abounada, and M. Ramzi, "Design of a PWM sliding mode voltage controller of a DC-DC boost converter in CCM at variable conditions," *Advances in Smart Technologies Applications and Case Studies*, vol. 684, pp. 263–270, 2019.
- [11] X. Sun, Z. Jin, L. Chen, and Z. Yang, "Disturbance rejection based on iterative learning control with extended state observer for a four-degree-of-freedom hybrid magnetic bearing system," *Mechanical Systems and Signal Processing*, vol. 153, Article ID 107465, 2021.
- [12] Y. Han, X. Wu, G. He, Y. Hu, and K. Ni, "Nonlinear magnetic field vector control with dynamic-variant parameters for high-power electrically excited synchronous motor," *IEEE Transactions on Power Electronics*, vol. 35, no. 10, Article ID 11053, 2020.
- [13] C. U. Reddy, K. K. Prabhakar, A. K. Singh, and P. Kumar, "Speed estimation technique using modified stator current error-based MRAS for direct torque controlled induction motor drives," *IEEE J. Emerg. Sel. Top. Power Electron*, vol. 8, pp. 1223–1235, 2019.
- [14] G. Foo and M. F. Rahman, "Sensorless sliding-mode MTPA control of an IPM synchronous motor drive using a sliding-mode observer and HF signal injection," *IEEE Transactions on Industrial Electronics*, vol. 57, no. 4, pp. 1270–1278, 2010.
- [15] M. Khan and S.-W. Kang, "Highly sensitive temperature sensors based on fiber-optic PWM and capacitance variation using thermochromic sensing membrane," *Sensors*, vol. 16, no. 7, p. 1064, 2016.
- [16] P. Naganathan and S. Srinivas, "Direct torque control techniques of three-level H-bridge inverter fed induction motor for torque ripple reduction at low speed operations," *IEEE Transactions on Industrial Electronics*, vol. 67, no. 10, pp. 8262–8270, 2020.
- [17] X. Wang, Z. Wang, Z. Xu, M. Cheng, and Y. Hu, "Optimization of torque tracking performance for direct-torque-controlled PMSM drives with composite torque regulator," *IEEE Transactions on Industrial Electronics*, vol. 67, no. 12, Article ID 10095, 2020.

- [18] L. Yu and D. Wang, "A hybrid filtering stage-based rotor position estimation method of PMSM with adaptive parameter," *Sensors*, vol. 21, no. 14, p. 4667, 2021.
- [19] B. Du, T. Zhao, S. Han, L. Song, and S. Cui, "Sensorless control strategy for IPMSM to reduce audible noise by variable frequency current injection," *IEEE Transactions on Industrial Electronics*, vol. 67, no. 2, pp. 1149–1159, 2020.
- [20] T. Wu, D. Luo, S. Huang et al., "A fast estimation of initial rotor position for low-speed free-running IPMSM," *IEEE Transactions on Power Electronics*, vol. 35, no. 7, pp. 7664–7673, 2020.
- [21] X. Sun, M. Wu, C. Yin, S. Wang, and X. Tian, "Multiple-iteration search sensorless control for linear motor in vehicle regenerative frequency suspension," *IEEE Transactions on Transportation Electrification*, vol. 7, no. 3, pp. 1628–1637, 2021.
- [22] C. M. Verrelli, S. Bifaretti, E. Carfagna et al., "Speed sensor fault tolerant PMSM machines: from position-sensorless to sensorless control," *IEEE Transactions on Industry Applications*, vol. 55, no. 4, pp. 3946–3954, 2019.
- [23] X. Sun, J. Cao, G. Lei, Y. Guo, and J. Zhu, "Speed sensorless control for permanent magnet synchronous motors based on finite position set," *IEEE Transactions on Industrial Electronics*, vol. 67, no. 7, pp. 6089–6100, 2020.
- [24] H. Zhang, W. Liu, Z. Chen et al., "A time-delay compensation method for IPMSM hybrid sensorless drives in rail transit applications," *IEEE Transactions on Industrial Electronics*, vol. 66, no. 9, pp. 6715–6726, 2019.
- [25] A. T. Woldegiorgis, X. Ge, S. Li, and M. Hassan, "Extended sliding mode disturbance observer-based sensorless control of IPMSM for medium and high-speed range considering railway application," *IEEE Access*, vol. 7, Article ID 175302, 2019.
- [26] J. Xu, Y. Du, H. Fang, H. Guo, and Y.-H. Chen, "A robust observer and nonorthogonal PLL-based sensorless control for fault-tolerant permanent magnet motor with guaranteed postfault performance," *IEEE Transactions on Industrial Electronics*, vol. 67, no. 7, pp. 5959–5970, 2020.
- [27] X. Wu, S. Huang, K. Liu et al., "Enhanced position sensorless control using bilinear recursive least squares adaptive filter for interior permanent magnet synchronous motor," *IEEE Transactions on Power Electronics*, vol. 35, no. 1, pp. 681–698, 2020.
- [28] G. Wang, D. Xiao, G. Zhang, C. Li, X. Zhang, and D. Xu, "Sensorless control scheme of IPMSMs using HF orthogonal square-wave voltage injection into a stationary reference frame," *IEEE Transactions on Power Electronics*, vol. 34, no. 3, pp. 2573–2584, 2019.
- [29] K. Scicluna, C. S. Staines, and R. Raute, "Sensorless position control at the steered wheel in steer-by-wire: using high-frequency injection with search-based observer," in *Proceedings of the 2020 IEEE 20th Mediterranean Electrotechnical Conference*, pp. 81–86, Palermo, Italy, June 2020.
- [30] R. Nair and G. Narayanan, "Stator flux based model reference adaptive observers for sensorless vector control and direct voltage control of doubly-fed induction generator," *IEEE Transactions on Industry Applications*, vol. 56, pp. 3776–3789, 2020.
- [31] Y. Wang, Y. Xu, and J. Zou, "ILC-based voltage compensation method for PMSM sensorless control considering inverter nonlinearity and sampling current DC bias," *IEEE Transactions on Industrial Electronics*, vol. 67, no. 7, pp. 5980–5989, 2020.
- [32] W. Xu, Y. Jiang, C. Mu, and F. Blaabjerg, "Improved nonlinear flux observer-based second-order SOIFO for PMSM sensorless control," *IEEE Transactions on Power Electronics*, vol. 34, no. 1, pp. 565–579, 2019.
- [33] D. Liang, J. Li, R. Qu, and W. Kong, "Adaptive second-order sliding-mode observer for PMSM sensorless control considering VSI nonlinearity," *IEEE Transactions on Power Electronics*, vol. 33, pp. 8994–9004, 2017.
- [34] Y. Wang, X. Wang, W. Xie, and M. Dou, "Full-speed range encoderless control for salient-pole PMSM with a novel full-order SMO," *Energies*, vol. 11, pp. 1–14, 2018.
- [35] A. Andersson and T. Thiringer, "Motion sensorless IPMSM control using linear moving horizon estimation with Luenberger observer state feedback," *IEEE Transactions on Transportation Electrification*, vol. 4, no. 2, pp. 464–473, 2018.
- [36] H. Yang, R. Yang, W. Hu, and Z. Huang, "FPGA-based sensorless speed control of PMSM using enhanced performance controller based on the reduced-order EKF," *IEEE Journal of Emerging and Selected Topics in Power Electronics*, vol. 9, no. 1, pp. 289–301, 2021.
- [37] E. Zerdali, "A comparative study on adaptive EKF observers for state and parameter estimation of induction motor," *IEEE Transactions on Energy Conversion*, vol. 35, no. 3, pp. 1443–1452, 2020.
- [38] X. Sun, C. Hu, G. Lei, Z. Yang, Y. Guo, and J. Zhu, "Speed sensorless control of SPMSM drives for EVs with a binary search algorithm-based phase-locked loop," *IEEE Transactions on Vehicular Technology*, vol. 69, no. 5, pp. 4968–4978, 2020.
- [39] W. El Merrassi, A. Abounada, and M. Ramzi, "Advanced speed sensorless control strategy for induction machine based on neuro-MRAS observer," *Materials Today: Proceedings*, vol. 45, pp. 7615–7621, 2021.